JACS
JOURNAL OF THE AMERICAN CHEMICAL SOCIETY
Article
pubs.acs.org/JACS

Plasmon-Enhanced Formic Acid Dehydrogenation Using Anisotropic Pd−Au Nanorods Studied at the Single-Particle Level

Zhaoke Zheng,[†] Takashi Tachikawa,[‡] and Tetsuro Majima*[,†]

[†]The Institute of Scientific and Industrial Research (SANKEN), Osaka University, Mihogaoka 8-1, Ibaraki, Osaka 567-0047, Japan
[‡]Department of Chemistry, Graduate School of Science, Kobe University, 1-1 Rokkodai-cho, Nada-ku, Kobe 657-8501, Japan

Supporting Information

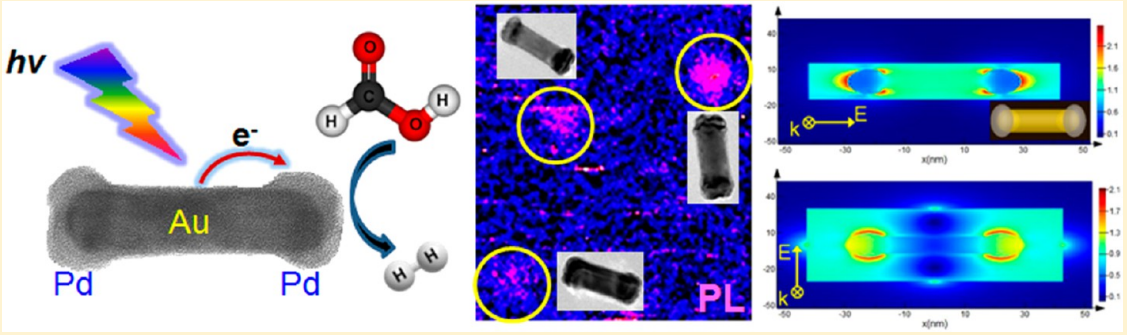

ABSTRACT: Plasmonic bimetal nanostructures can be used to drive the conventional catalytic reactions efficiently at low temperature with the utilization of solar energy. This work developed Pd-modified Au nanorods, which work as the light absorber and the catalytically active site simultaneously, and exhibit efficient plasmon-enhanced catalytic formic acid dehydrogenation even when below room temperature (5 °C). Plasmon-induced interface interaction and photoreaction dynamics of individual nanorods were investigated by single-particle photoluminescence measurement, and a complete quenching phenomenon at the LSPR region was observed for the first time. More importantly, the spatial distribution of the SPR-induced enhancement, analyzed by the finite difference time domain (FDTD) simulation, shows that only tip-coated Pd can be affected for the occurrence of plasmon resonance energy transfer. This finding provides a route to decrease the amount of Pd species by the selective deposition only at the field-enhanced sites.

INTRODUCTION

Solar energy is a promising energy source due to its clean and abundant properties. Among various solar harvesting technologies, the utilization of solar energy to drive the conventional catalytic chemical transformation has received significant attention.[1−3] Plasmonic metal nanostructures can harvest visible light efficiently by their strong interaction with resonant photons through an excitation of surface plasmon resonance (SPR).[4,5] Surface plasmons (SPs) decay by either elastic radiative re-emission of photons or the formation of energetic hot electrons. The electrons can be transferred to the adsorbate acceptor states or relax by locally heating the nanostructure.[6−8] Thus, the excited plasmonic nanostructures can be employed to enhance the conventional heterogeneous catalysis.

Hydrogen storage and production are of great importance for electricity generation in fuel cells.[9] Formic acid (HCOOH) has been widely used as a liquid storage medium capable of releasing H_2 via the catalytic dehydrogenation. Nevertheless, the activity and selectivity strongly depend on the temperature, and in practice, the outdoor temperature is even lower than room temperature (usually 20−25 °C). Despite increasing interest in enhancing the H_2 production from formic acid at room temperature,[9,10] little effort has been devoted to utilizing light energy to boost the catalytic dehydrogenation. Pd is one of the most active catalysts for formic acid dehydrogenation;[10] unfortunately, the absence of strong SPR absorption over Pd inhibited the light energy utilization. Au nanorods (NRs), with broadly tunable aspect-ratio-dependent longitudinal SPR (LSPR), exhibit a wide range of visible-light harvesting.[11] Thus, when coupled with Pd, the Pd−Au bimetal heterostructures will simultaneously act as the light absorber and the catalytically active site.

To boost formic acid dehydrogenation, it has been reported that the charge transfer within bimetallic nanostructures (owing to the work function difference) could strengthen the adsorption of formate, and hence enhance the rate of hydrogen production.[9,12,13] It is also reported that the surface charge heterogeneity of bimetallic nanoparticles (NPs) could enhance the catalytic activity.[14] In the Pd−Au case, the hot electrons generated by SP decay may transfer from Au to Pd sites, and hence potentially enhance the surface charge heterogeneity. Some efforts have been devoted to plasmonic harvesting of light energy for driving thermal catalysis with bimetallic

Received: November 14, 2014
Published: December 26, 2014

DOI: 10.1021/ja511719g
J. Am. Chem. Soc. 2015, 137, 948−957

nanostructures.[2,14,15] However, the detailed mechanism of plasmon-induced contribution is still ambiguous, especially for the interfacial interaction between the two metal segments, which was thought to be the crucial factor for the enhanced activity.[2,14,16] Therefore, unraveling the plasmon-induced interfacial interaction within bimetal nanostructures is essential to understand the plasmon-enhanced mechanism.

Due to the heterogeneity of chemically synthesized nanostructures, single-particle spectroscopy[17] correlated with high-resolution morphological characterization is very necessary. We initially developed this technique, namely, correlated single particle spectroscopy and HRTEM, to study the photocatalytic water splitting process of Pt−Au NRs,[18] and the analysis indicates the electron transfer from Au to Pt. However, the mechanism of plasmon-enhanced thermal catalysis, different with the photoctalytic process, is still ambiguous. For the photocatalytic process, both Au NR and Pt play a part in the photocatalytic oxidation and reduction processes, respectively. In the Pd−Au case, only the Pd segment acts as an active thermal catalyst for the formic acid dehydrogenation, while the Au NR acts as an adjuvant. Herein, this technique was applied to unravel the nature of plasmon-enhanced thermal catalysis using Pd−Au NRs, and confirmed the plasmon-induced interfacial interaction within these bimetal nanostructures. Moreover, the sensitivity of single-particle photoluminescence (PL) measurement is not high enough for measuring the core−shell sample with low PL intensity in our previous work.[18] In the present study, we developed the single-particle PL measurement with higher sensitivity and observed the complete quenching phenomenon at the LSPR region for the first time. Different from the reported Pd−Au NRs,[15] herein we synthesized anisotropic Pd-tipped and Pd-covered Au NRs. Such bimetallic nanostructures can utilize solar energy to drive catalytic formic acid dehydrogenation even below room temperature (5 °C) with high performance comparable with the conventional thermal catalysis at 40 °C. More importantly, the finite difference time domain (FDTD) simulation was carried out to analyze the spatial distribution of the SPR-induced enhancement. The result shows that, if plasmon resonance energy transfer occurs, only tip-coated Pd can be affected, providing a route to decrease the amount of Pd species by selective deposition only at the field-enhanced sites.

EXPERIMENTAL SECTION

Preparation of Au NRs. Pure Au NRs were synthesized by the seed-mediated method.[19,20] Briefly, the seed solution was made by adding a freshly prepared, ice-cold aqueous solution of $NaBH_4$ (Sigma-Aldrich, 0.6 mL, 0.01 M) into a mixture solution composed of $HAuCl_4{\cdot}3H_2O$ (Sigma-Aldrich, 29 μL, 0.086 M) and CTAB (TCI, 10 mL, 0.1 M). The solution was stirred vigorously (1200 rpm) for 2 min and aged at room temperature for 30 min before use.

The growth solution was prepared by dissolving CTAB (3.6 g) and 5-bromosalicylic acid (Wako Pure Chemical Industries, 0.44 g) in 100 mL of warm water (Millipore, 55 °C). To this solution, 1.92 mL of 0.01 M fresh $AgNO_3$ (Sigma-Aldrich) was added, and after keeping it undisturbed at 25 °C for 15 min, 100 mL of 1 mM $HAuCl_4{\cdot}3H_2O$ solution was added. After gentle mixing of the solution for 15 min, 0.512 mL of 0.1 M ascorbic acid (Nacalai Tesque) was added with vigorously stirring for 30 s until the mixture became colorless. At this point, 0.32 mL of seed solution was added to the entire growth solution. The mixture was stirred for 30 s and left undisturbed at 27 °C for 12 h. The color of the growth solution slowly changed from colorless to violet, indicating the growth of Au NPs. The as-made Au NRs were labeled as Au-NRs-1 and used for subsequent Pd deposition on this Au NR template without purification treatment. Another Au NR template, labeled as Au-NRs-2, was also made following a similar procedure except eliminating 5-bromosalicylic acid and increasing the concentration of CTAB to 0.1 M.

Preparation of Pd−Au NRs. H_2PdCl_4 solution (0.01 M) was prepared by dissolving 0.089 g of $PdCl_2$ powder in 50 mL of 0.02 M HCl solution at 60 °C. Pd-tipped Au NRs were prepared by using Au-NRs-1 as a template similar to our former work.[18] Briefly, 1.136 mL of 0.1 M ascorbic acid was added into 10 mL of as-made Au-NRs-1 suspension. Then, 198 μL of 0.01 M H_2PdCl_4 and subsequently 80 μL of 0.1 M HCl (Wako Pure Chemical Industries) were added to the reaction mixture. The mixture was left undisturbed for 12 h at 27 °C. Pd-covered Au NRs were prepared by using Au-NRs-2 as a template following the same procedure.

Preparation of Pt-Tipped Au NRs. Pt-tipped Au NRs were prepared following the method reported in our previous paper.[18] Briefly, 0.568 mL of 0.1 M ascorbic acid was added into 10 mL of Au-NRs-1 suspension. Then, 99 μL of 0.01 M $H_2PtCl_6{\cdot}6H_2O$ and subsequently 0.08 mL of 0.01 M HCl were added to the reaction mixture. The mixture was left undisturbed for 12 h at 27 °C.

Preparation of Au Nanospheres (NSs). A solution of $HAuCl_4{\cdot}3H_2O$ (2 mL, 1 wt %) was dissolved in 99 mL of Milli-Q ultrapure water in a three-neck round-bottom flask and heated to 100 °C. Under vigorous stirring, sodium citrate (Wako Pure Chemical Industries, 1.2 mL, 1 wt %) was added and the reaction mixture was maintained at the boiling temperature for a further 30 min before cooling to room temperature.

Characterization of Materials. Transmission electron microscopy (TEM) and high-resolution transmission electron microscopy (HRTEM) measurements were carried out on a JEOL-2100 instrument operated at 200 kV and a JEM-3000F instrument operated at 300 kV (JEOL). Scanning TEM (STEM) and energy dispersive spectroscopy (EDS) mapping were performed using a Cs-corrected JEM-ARM200F microscope operated at 200 kV. Extinction spectra were taken using quartz cuvettes of 1 cm path length on a Shimadzu UV-3600 UV−vis−NIR spectrophotometer.

FDTD Calculations. The computational simulations were performed by using the finite-difference-time-domain (FDTD) method with perfectly matched layers (PML) boundary conditions. A software package, FDTD Solutions (Lumerical Solutions, Inc.), was employed to perform FDTD calculations. The optical constants of Au were adopted from tabulated values for bulk gold measured by Johnson and Christy.[21] The size of the NRs was taken to match their average values. Specifically, the Au NR was modeled as a cylinder capped with two half-spheres at the ends, with a length of 50 nm and a diameter of 14 nm. For the model of Pd-tipped Au NR, ellipse Pd spheres with diameters of 14 and 20 nm were located at both ends of the Au NR with a total length of 58 nm. For the model of the Pd-covered Au NR, a thin layer Pd with a thickness of 2 nm was homogeneously located on the surface of the Au NR. The boundary with NRs inside was divided into meshes of 0.5 nm in size. For NRs dispersed in aqueous solutions, the refractive index of the medium was set to be 1.33.

Hydrogen Production from Formic Acid. The aqueous suspensions of nanorods were centrifuged at 12 000 rpm to remove excess surfactant, washed with Milli-Q ultrapure water two times, and finally redispersed in Milli-Q ultrapure water.

The catalyst suspensions were mixed with 4 mL of formic acid (1 M) and sealed with a rubber septum. For visible-light hydrogen production, the suspensions were irradiated with visible light (Asahi Spectra, LAX-C100; 100 mW cm^{-2}) with magnetic stirring. A 460 nm cutoff filter was used to remove UV light. The temperature of the reaction system was carefully controlled with a water bath. The reaction system under dark and light irradiation was maintained at the same temperature to ensure that the comparison is meaningful. The amount of H_2 in the gas phase was measured using a Shimadzu GC-8A gas chromatograph equipped with an MS-5A column and a thermal conductivity detector (TCD). To obtain an action spectrum in this reaction system, H_2 formation in an aqueous suspension of the catalyst was carried out under the irradiation of monochromated visible-near-infrared light from a Xe lamp (Asahi Spectra, HAL-320W; 4.8 mW

DOI: 10.1021/ja511719g
J. Am. Chem. Soc. 2015, 137, 948−957

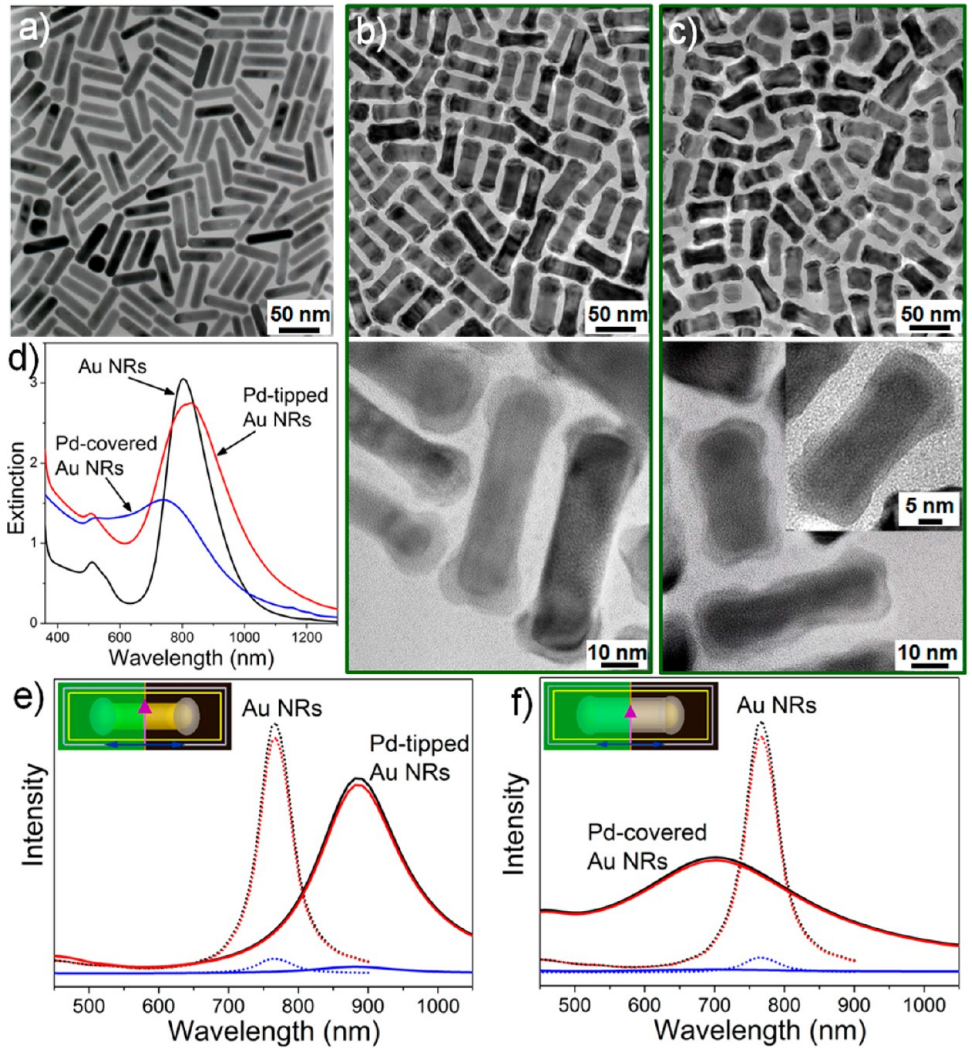

Figure 1. (a–c) TEM images of Au NRs (a), Pd-tipped Au NRs (b), and Pd-covered Au NRs (c). (d) UV–vis–NIR extinction spectra of the three samples with the same total mass. (e and f) Calculated extinction spectra for Au NRs and Pd–Au NRs using the FDTD method. Both samples were dispersed in aqueous solutions, and the refractive index of the surrounding medium was taken to be 1.33. The black, red, and blue colors represent extinction, absorption, and scattering spectra, respectively.

cm^{-2}) equipped with 29 different bandpass filters (Thorlabs, 10 nm fwhm) at different wavelengths.

Catalytic Reduction of 4-Nitrophenol (4-NP). The aqueous suspensions of NRs were washed with Milli-Q ultrapure water two times, further treated with 60% $HClO_4$ under ultrasonic conditions for 5 min to remove the bilayer surfactant adhered onto Au NRs, and then thoroughly washed and redispersed in equivalent Milli-Q ultrapure water. The rate of 4-NP reduction was evaluated using UV–vis spectroscopy (Shimadzu UV-3600). For this propose, the catalyst suspension was mixed with an aqueous solution of 4-NP (4 mL, 0.4 mM) and freshly prepared $NaBH_4$ (0.1 mL, 0.1 M) at room remperature. For the visible-light catalytic reduction, the suspensions were irradiated with visible light (Asahi Spectra, LAX-C100; 100 mW cm^{-2}) without stirring. A 520 nm cutoff filter was used to obtain the visible light.

Sample Preparation for Single-Particle PL Experiments. The quartz cover glasses were purchased from DAICO MFG CO., Ltd. (Japan), and cleaned by sonication in a 20% detergent solution (As One, Cleanace) for 6 h, followed by repeated washings with warm water five times, and finally stored in Milli-Q ultrapure water (Millipore). TEM Windows Grids (ALLIANCE Biosystems, silicon oxide 40 nm membrane, frame thickness of 100 μm) were cleaned with O_3 for 50 cycles, and then, the surface was deposited with a layer of Al_2O_3 with a thickness of 5 nm by atomic layer deposition (ALD) at 150 °C to decrease the background noise during the single-particle PL measurements. Pd-tipped Au NR and pure Au NR aqueous suspensions were centrifuged at 12 000 rpm (Hitachi, himac CF16RX) to remove excess surfactant and then redispersed in Milli-Q ultrapure water. The well-dispersed aqueous suspensions of NRs were spin-coated on the ALD-treated TEM grid. The grid was mounted on the top of a stainless steel holder upside-down. A cleaned quartz cover glass was placed on the particle-coated grid to form a sandwich structure, and a cap with an O-ring seal was tightly screwed to fix this structure.

Single-Particle PL Measurements by Confocal Microscopy. Single-particle PL images and spectra were recorded by using an objective scanning confocal microscope system (PicoQuant, MicroTime 200) coupled with an Olympus IX71 inverted fluorescence microscope. The samples were excited through an oil-immersion objective lens (Olympus, UplanSApochromat, 100×, 1.4 NA) with a circular-polarized 405 nm continuous wave (CW) laser controlled by a PDL-800B driver (PicoQuant). Typical excitation powers for the PL measurements were 300 μW at the sample. The emission from the sample was collected by the same objective and detected by a single-photon avalanche photodiode (Micro Photon Devices, PDM 50CT) through a dichroic beam splitter (Chroma, 405rdc) and long pass filter (Chroma, HQ430CP). For the spectroscopy, only emission that passed through a slit entered the imaging spectrograph (Acton

DOI: 10.1021/ja511719g
J. Am. Chem. Soc. 2015, 137, 948–957

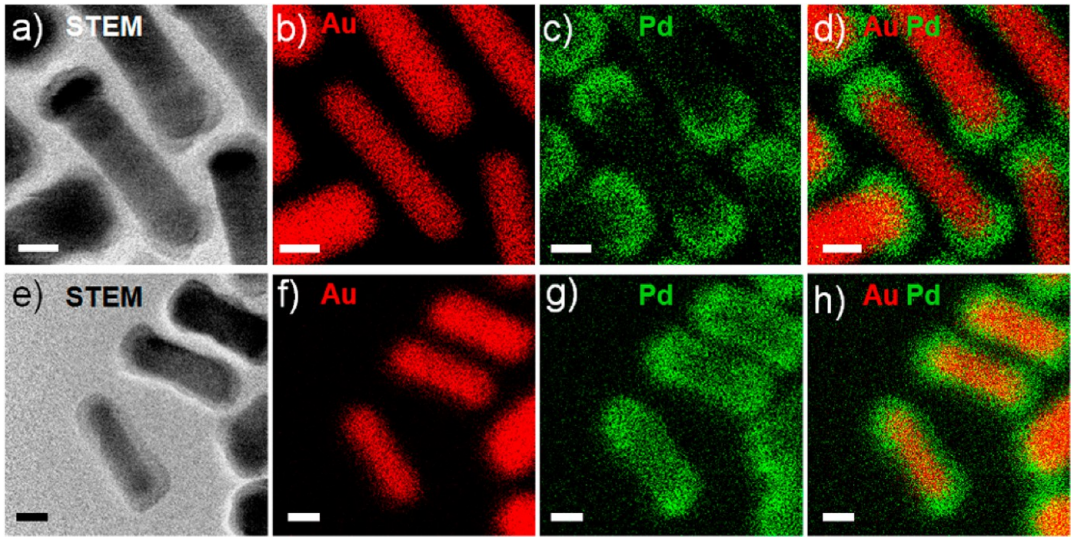

Figure 2. STEM images and corresponding STEM-EDS elemental maps of Au, Pd, and Au + Pd: (a–d) Pd-tipped Au NRs; (e–h) Pd-covered Au NRs. The scale bars in all images represent 10 nm.

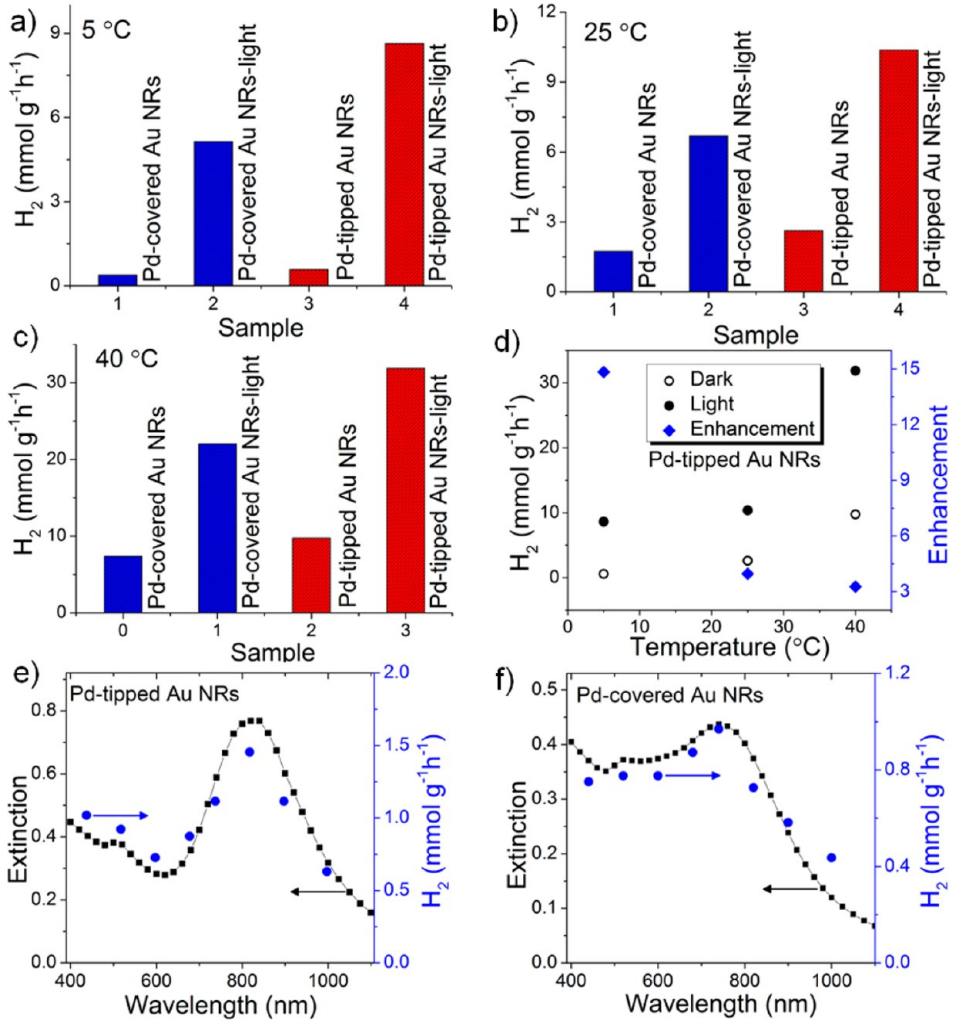

Figure 3. (a–c) The rate of H_2 evolution from formic acid suspensions of Pd–Au NRs under the dark and visible-light irradiation (λ > 460 nm, 100 mW cm^{-2}) at 5 (a), 25 (b), and 40 °C (c). (d) The rate (left axis) and temperature enhancement (right axis) of H_2 evolution under the dark and light irradiation (λ > 460 nm) over Pd-tipped Au NRs. (e and f) Extinction spectra (left axis) and action spectra of H_2 evolution rates under the nearly monochromatic light irradiation with an intensity of 4.8 mW cm^{-2} (right axis).

DOI: 10.1021/ja511719g
J. Am. Chem. Soc. 2015, 137, 948–957

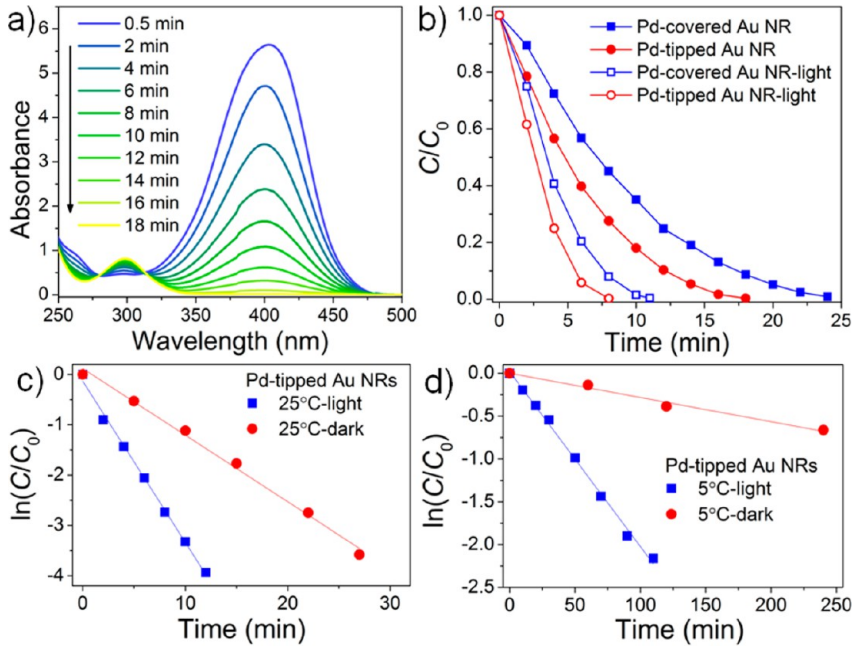

Figure 4. (a) Time-dependent UV−vis absorption spectra of the reduction of 4-nitrophenol (4-NP) by $NaBH_4$ in the presence of Pd-tipped Au NRs (0.008 mg) in the dark at 25 °C. (b) Time-dependent profiles for this catalytic reaction with or without light irradiation (λ > 520 nm) at 25 °C. (c and d) Kinetic linear fitting curves for the reduction of 4-NP over Pd-tipped Au NRs at 25 and 5 °C.

Research, SP-2356) that was equipped with an electron-multiplying charge-coupled device (EMCCD) camera (Princeton Instruments, ProEM). The spectra were typically integrated for 20 s.

RESULTS AND DISCUSSION

Figure 1a shows transmission electron microscopy (TEM) images of the pure Au NRs. The NRs have an average aspect ratio of 3.9 ± 0.3, and they give rise to a LSPR peak centered at about 804 nm (Figure 1d). Anisotropic overgrowth of Pd on Au NRs was obtained using a modified two-step seed-mediated growth method. As shown in Figure 1b, cap-shaped Pd nanocrystals were selectively deposited at the tips of Au NRs, named as Pd-tipped Au NRs. Figure 1c shows the TEM images of Pd-covered Au NRs, which were synthesized by altering the side-coating surfactants. A thin layer of Pd with a thickness of 2 nm was homogeneously deposited on the surface of the Au NR and shows a layered growth pattern (Frank−van der Merwe mode).[22] High-resolution TEM (HRTEM) images (Figures S1 and S2, Supporting Information) of both samples exhibit coherent lattice fringes with a single crystalline structure, suggesting an epitaxial growth of Pd on Au NRs.[23] The clear fringes in the Pd and Au regions show periods of 1.95 and 2.04 Å, as expected for face-centered cubic (fcc) Pd(200) and Au(200) planes, respectively. The extinction spectrum of the Pd-tipped sample (Figure 1d) shows a little red-shift of the LSPR peak because of the relative changes in the aspect ratio after tip-coating.[24] However, for the Pd-covered sample, a decrease in LSPR intensity was observed because of the complete encapsulation of the Au NR core by the Pd shell.[25] We further carried out FDTD calculations on Pd−Au NRs that dispersed in aqueous solutions with a refractive index of 1.33. The FDTD technique can provide a full range of SPR-related properties including extinction, scattering cross sections, and local electric fields. As shown in Figure 1e and f, the calculated extinction spectra from FDTD simulation of both samples exhibit consistent peak shift and broadening, which are in agreement with those from experimental measurements.

To further examine the distribution of Pd on Au NRs, we preformed scanning TEM (STEM) and energy dispersive spectroscopy (EDS) analysis on Pd-tipped and Pd-covered Au NRs (Figure 2). From the EDS elemental maps of Pd-tipped Au NRs (Figure 2b−d), we can clearly see that the Pd was only located at the tips of Au NRs while there is no Pd shell in the middle part of the Au NRs, which confirmed the tip-coated nanostructure. As for Pd-covered Au NRs, the elemental maps (Figure 2f−h) show that a layer of Pd shell was homogeneously deposited on the surface of the Au NR, which is consistent with the HRTEM analysis.

The anisotropic heterostructure of the Pd−Au NRs offers the possibility of plasmon-enhanced catalytic applications using the wide range of visible−NIR light as well as the elucidation of the effect of different plasmon modes on the properties. Parts a−c of Figure 3 show the reaction rate of the H_2 evolution from formic acid dehydrogenation under the dark and light irradiation at different temperatures. The reaction system under the dark and light irradiation was maintained at the same temperature controlled by a water bath to ensure that the comparison is meaningful. Without light irradiation, the activities for both samples are very low at 5 °C, because the thermocatalytic formic acid dehydrogenation is greatly suppressed at such a low temperature. However, with light irradiation, the H_2 evolution rate over Pd-tipped Au NRs increased nearly 15 times compared with that under the dark (conventional thermal catalysis). To the best of our knowledge, this is the first report about the H_2 generation from formic acid working at such a low temperature (5 °C), which is comparable to the outside temperature of most areas in the winter. Thus, the plasmon-enhanced catalysis may enable us to use the fuel cell devices outdoors even in the winter. The H_2 evolution rate at 5 °C under the visible-light irradiation was even comparable with that of the conventional thermal catalysis (in dark) at 40

DOI: 10.1021/ja511719g
J. Am. Chem. Soc. 2015, 137, 948−957

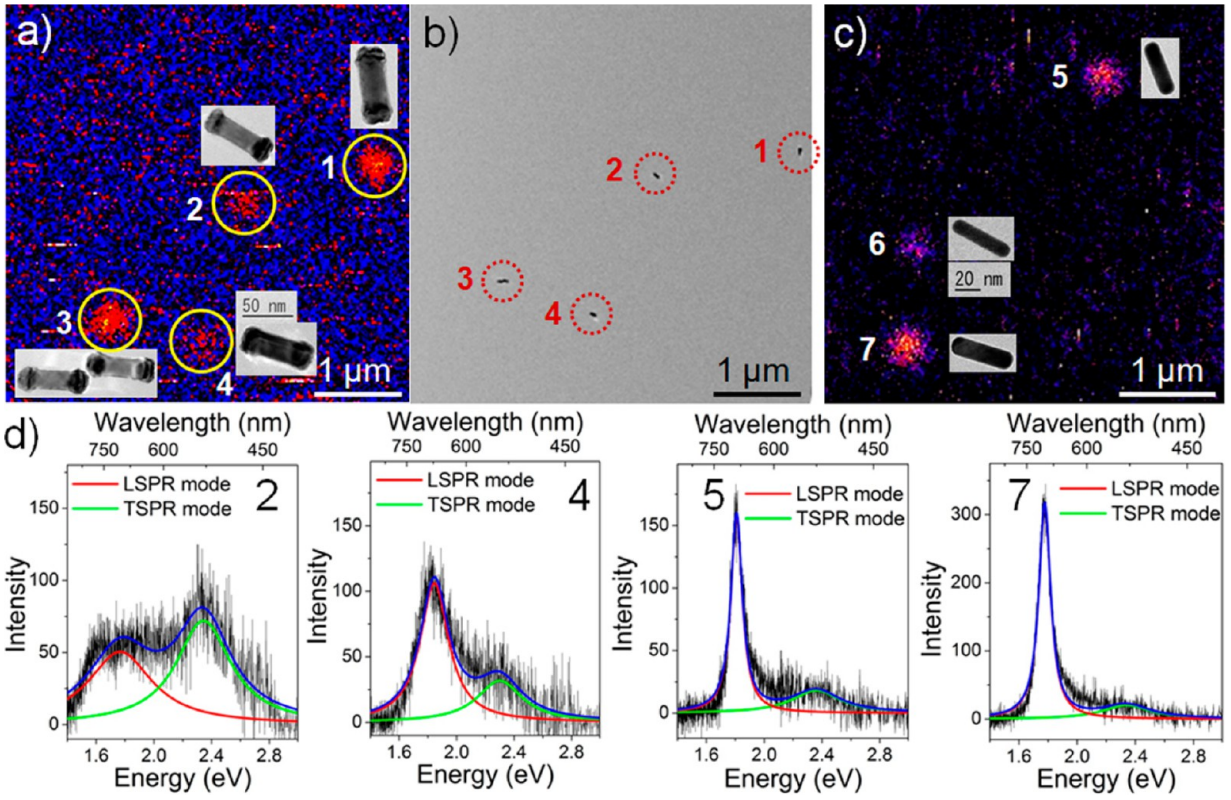

Figure 5. (a and c) PL image of individual Pd-tipped Au NRs (a) and pure Au NRs on SiO_2-TEM-grid (c). Correlated high magnification TEM images are shown next to the PL signal. (b) Low-magnification TEM image of individual Pd-tipped Au NRs for the same area in Figure 3a. (d) PL spectra of the corresponding single Pd-tipped Au NR and pure Au NR as numbered in the PL image.

°C using the same catalyst (Figure 3a and c). The turnover frequency (TOF, defined as mol of H_2/mol of total Pd catalyst) over Pd-tipped Au NRs without any additive was measured to be 13.7 h^{-1} at 5 °C under the light irradiation. Although this TOF value was lower than that of the highest value, 80 h^{-1}, reported by Jiang's group,[12] their result was obtained at room temperature. Meanwhile, the activity may be further enhanced by increasing the surface area of Pd through island growth pattern (Volmer–Wever mode) in the future, which generates tiny Pd NPs.

The activity for the Pd-covered sample under the light irradiation was also largely enhanced compared with the conventional thermal catalysis. These results clearly show that the light energy could efficiently drive the conventional catalytic reaction. With increasing reaction temperature, the activities for both samples increased correspondingly, due to the increased thermocatalytic contribution. Notably, the Pd-tipped Au NRs show a much higher activity compared to the Pd-covered sample under the same conditions, indicating that the anisotropic tip-coated nanostructure with greater surface charge heterogeneity is more favorable for the catalytic reaction. No CO was detected, and the activity of H_2 evolution over pure Au NRs (Figure S3, Supporting Information) was negligible in our result. The activity enhancement, calculated as the H_2 evolution rates under the light irradiation divided by that under the dark, decreased as a function of temperature from about 15-fold to 3-fold for the Pd-tipped sample (Figure 3d). Similar results were also observed for the Pd-covered sample (Figure S4, Supporting Information), again indicating that the light energy could effectively drive the formic acid dehydrogenation even at low temperature while the thermocatalysis was almost inoperative. To confirm that the light-enhanced catalytic performance is due to the plasmonic resonance effect, we further investigated the H_2 evolution action spectrum using nearly monochromatic light with a width of ±5 nm and intensity of 4.8 mW cm^{-2} at 5 °C. As shown in Figure 3e and f, the action spectra are in agreement with the extinction spectra of Pd–Au NRs, clearly demonstrating that the enhanced H_2 evolution from formic acid dehydrogenation was induced by the SPR excitation of Au NRs.

To confirm the generality of such plasmon-enhanced catalytic reaction, the reduction of 4-NP by $NaBH_4$ in the presence of Pd–Au NRs with or without light irradiation was also carried out. This reaction is often chosen as a model reaction to evaluate the catalytic activities of metal NPs.[26] As shown in Figure 4a and b and Figure S5 (Supporting Information), for both samples, the catalytic activity greatly increased with visible light irradiation, and the Pd-tipped Au NRs exhibit a relative higher performance. The influence of reaction temperature was also studied over Pd-tipped Au NRs (Figure 4c and d and Figure S6, Supporting Information). At 5 °C, the first-order kinetic rate constant of the Pd-tipped sample was 0.003 and 0.02 min^{-1} under the dark and light irradiation, respectively, indicating an enhancement of 6.7-fold was obtained by light energy. For the catalytic reduction of 4-NP, Yang et al. also observed an improved catalytic activity over Ag-tipped Au NRs.[27] They attributed this enhancement to the electronic effect. Toshima and co-workers further suggested that the electronic charge would transfer from Ag to Au, thereby improving the catalytic activity.[28,29] Thus, the interfacial interaction between the two metal segments is essential for the improved catalysis.

DOI: 10.1021/ja511719g
J. Am. Chem. Soc. 2015, 137, 948–957

For the catalytic reduction of 4-NP, it is well-known that the metal NPs catalyze this reaction by facilitating electron relay from the donor BH_4^- to the acceptor 4-NP to overcome the kinetic barrier.[30] Metal NPs react with BH_4^- to form the metal hydride, while at the same time 4-NP adsorbs onto the metal surface. In our case, the hot electrons transfer from Au to Pd, enhancing the surface charge heterogeneity. It has been reported that greater surface charge heterogeneity results in an enhanced interaction between adsorbate and metal NPs.[14] The spatial separation of electrons and holes as well as coexposed Pd and Au surfaces in Pd-tipped Au NRs result in a greater surface charge heterogeneity, and hence an improved catalytic activity.

Recently, there have been some reports on merging the field of SPR and conventional catalysis using bimetallic nanostructures. However, the detailed mechanism of bimetallic interfacial interaction is still ambiguous. Such an interfacial interaction is the crucial factor for the plasmon-enhanced catalytic reaction. To unravel the mechanism of plasmon-enhanced catalysis, we investigated the light-induced interfacial interaction between the Au NRs and Pd by single-particle PL spectroscopy combined with TEM. Parts a and b of Figure 5 show a typical single-particle PL image of individual Pd-tipped Au NRs and the low-magnification TEM image for the same area; the high-magnification TEM images of the corresponding NRs are also displayed next to the PL signal. The individual Au NRs were also investigated, as shown in Figure S7 (Supporting Information). The PL spectra of individual Pd-tipped Au NRs and pure Au NRs, collected by switching the detection to a spectrometer equipped with an electron-multiplying charge-coupled device (EMCCD) camera, are shown in Figure 5d. PL intensities at the LSPR and transversal SPR (TSPR) regions were obtained by fitting the spectra with Lorentzian lineshapes. By comparing the PL spectra between Pd-tipped Au NRs and pure Au NRs, we found that the LSPR PL intensity of the Pd-tipped samples dramatically decreased compared to Au NRs, indicating that PL at the LSPR region was quenched by the tip-coated Pd.

Using the same method, we obtained tens of PL spectra of single Pd-tipped Au NRs combined with morphological characterization, and nine representative PL spectra with the corresponding TEM images are shown in Figure S8 (Supporting Information). The TSPR PL intensity is related to the volume of the Pd–Au NR, while the LSPR PL intensity is determined by the morphology due to the heterogeneity of the chemically synthesized nanostructures.[18] Although all NRs show tip-coated morphology and no laterally covered Pd NPs can be visually observed, the difference of the LSPR PL intensity may be attributed to the trace amounts of Pd on the lateral sites. This single-particle PL measurement can further be used to investigate other Au nanostructures, such as nanospheres (Figure S9, Supporting Information), nanocubes, and polyhedral Au–Pd core–shell particles,[31] which can give us some fundamental information on plasmon decay at the single-particle level.

By analyzing the PL spectra for 37 individual NRs (Figures S8 and S10, Supporting Information), we obtained the PL intensities as a function of diameter for individual Au NRs and Pd-tipped Au NRs (Figure 6a). As can be seen, the LSPR PL intensity of the Pd-tipped Au NRs dramatically decreased, while the TSPR PL intensity was similar for both samples. This demonstrates that PL at the LSPR mode was quenched by the Pd segment. The quenching efficiency of the individual Pd–Au

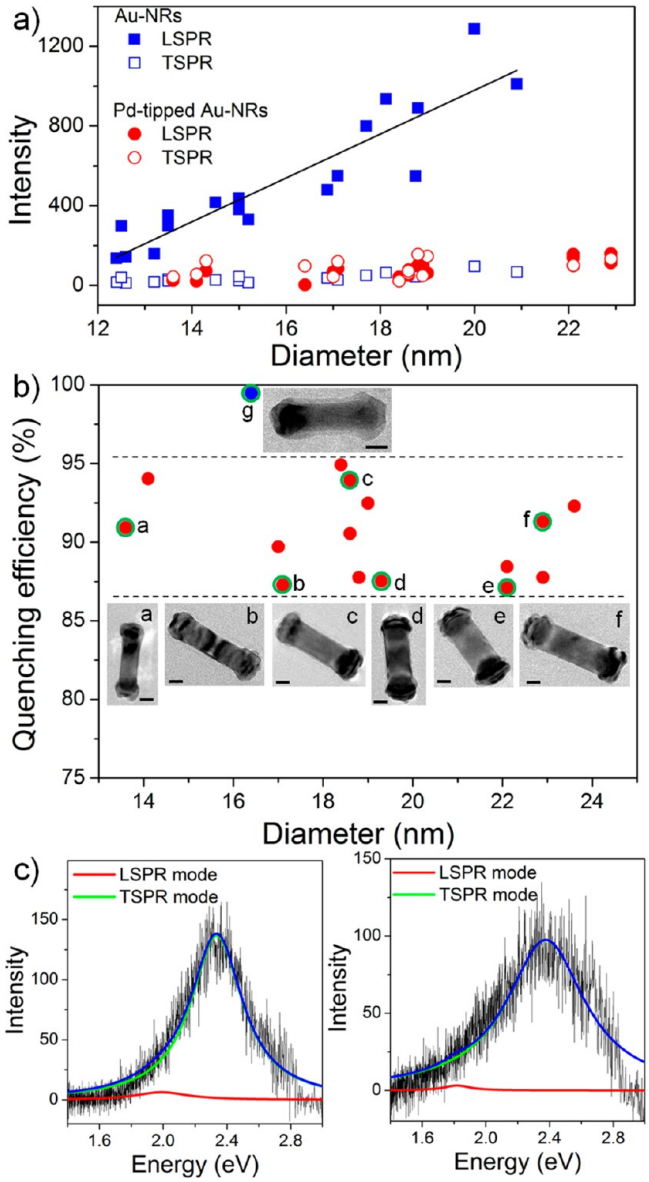

Figure 6. (a) PL intensities as a function of diameter for individual Au NRs and Pd-tipped Au NRs. (b) PL quenching efficiency of individual Pd-tipped (red dots) and Pd-covered (blue dots) Au NRs. Correlated TEM images for the circled points with the green outline are shown in the inset. Scale bars in the insets represent 10 nm. (c) PL spectra of two representative individual Pd-covered Au NRs.

NRs was calculated by comparing the LSPR PL intensities of both samples with the same diameter (Figure 6b). As shown in Figure 6b, the quenching efficiencies of the Pd-tipped sample mainly focused in the region of 87–95% (red dots in Figure 6b), while, for the Pd-covered sample, the quenching efficiency was nearly 100% (blue dots in Figure 6b), which was attributed to the fully covered Pd shell. Furthermore, we analyzed several more spectra of individual Pd-covered Au NRs, and found that the PL at the LSPR region was all nearly completely quenched (Figure 6c and Figure S12, Supporting Information). Notably, the complete quenching phenomenon was observed for the first time.

The luminescence of Au NRs is assigned to the radiative decay of SPs, and it occurs from both the TSPR and LSPR with the latter being the dominant decay route.[32,33] Figure S13

DOI: 10.1021/ja511719g
J. Am. Chem. Soc. 2015, 137, 948–957

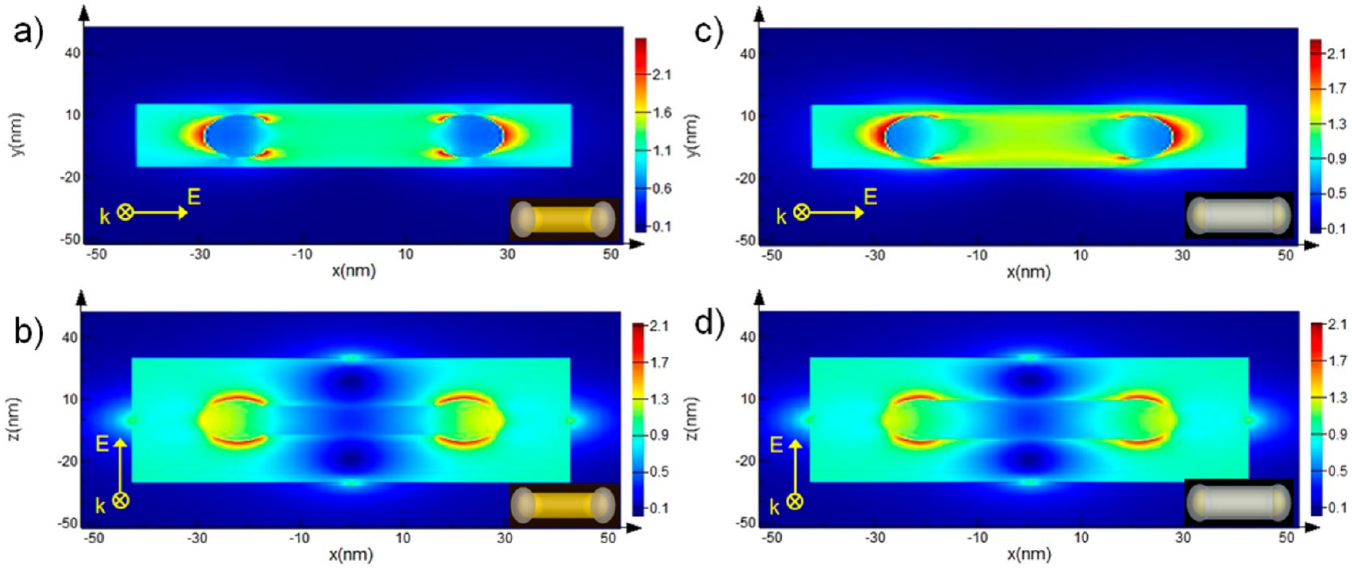

Figure 7. Spatial distribution of the SPR-induced enhancement of electric field intensity from FDTD simulation for Pd-tipped Au NRs (a and b) and Pd-covered Au NRs (c and d). Here *E* denotes the vector of the electric field and *k* denotes the wavevector.

(Supporting Information) shows the mechanism for plasmon emission of Au NRs. At 405 nm, the interband transition is excited, which creates electron−hole pairs that can relax efficiently through the nonradiative route. A fast interconversion also occurs between electron−hole pairs and the TSPR that subsequently decays radiatively, leading to the short-wavelength PL peak.[18,33] Meanwhile, the electrons which excited directly or generated from the TSPR lose energy by nonradiative decay and interconvert to the LSPR mode, which emits a photon via the radiative decay, leading to the long-wavelength PL peak. For the Pd−Au NRs, the hot electrons transfer from Au to Pd, generating a charge-separated (CS) state, which competes with the LSPR emission, leading to PL damping.[18] Therefore, the strong quenching of emission at the LSPR region confirmed the electron transfer from Au to Pd, giving rise to enhanced surface charge heterogeneity. As has been reported, such a charge transfer and charge redistribution enhance the interaction between the adsorbate and the catalyst, and thus enhance the catalytic activity.[12,16] The spatial separation of electrons and holes in the Pd-tipped sample results in an efficient charge separation, and hence an improved catalytic performance. For the Pd-covered Au NRs, the PL was completely quenched (100%), while the quenching was slightly less efficient (87−95%) for the Pd-tipped Au NRs, which means a less efficient electron transfer. Meanwhile, the charge recombination more efficiently occurs for the Pd-covered Au NRs because of the homogeneous coating of the Pd shell, which explains the comparable light-driven enhancement factor for both samples. To investigate the role of photogenerated holes in this catalytic process, the H_2 evolution over Pt-tipped Au NRs (Figure S14, Supporting Information) under the light irradiation was also examined. The rate was 96 μmol g^{-1} h^{-1} at 25 °C, much lower than 10 mmol g^{-1} h^{-1} for Pd-tipped Au NRs under the same conditions (Figure 3b). For Pt-tipped Au-NRs, the hot electrons can also transfer from Au to Pt, similar to the Pd case. If the holes play a key role in this formic acid dehydrogenation, the activity should also be high over Pt−Au NRs. The much lower activity of Pt−Au NRs demonstrates that the formic acid dehydrogenation is mainly attributed to the intrinsically catalytic prosperity of Pd.

The hot electrons, generated from SP decay, can also relax by locally heating the nanostructure, namely, SPR-induced photothermal heating. Usually, high-intensity visible lasers,[6,34,35] even a low-intensity NIR laser,[15] or a Xe lamp under gas-phase conditions[36,37] induce effective local heating of the nanostructures and thereby facilitate thermocatalytic reaction. In our case, low-intensity visible photons (comparable to solar intensity) were used to drive the plasmon-enhanced reaction; moreover, the reaction was carried out in the aqueous phase and the temperature was kept constant controlled by the water bath. Up to now, a viable experimental approach for directly probing the SPR-induced local temperature within the nanometer size regime still remains limited.[34] Govorov's group has calculated the surface temperature increase for a series of Au NPs immersed in water as a function of illumination power; it has been shown that, even when the illumination intensity reached 10^3 W cm^{-2}, the temperature increase at the surface of a 50 nm Au NP was less than 1 K.[35,38] Even with a high-intensity pulse laser, the temperature increase over the Au NR is only ∼5.5 K.[39] Using Green's dyadic method, Baffou's group performed the simulation of heat-density distribution on the Au NR. Unexpectedly, the heat generation mainly arises from the center part of the nanorod.[40] If so, the Pd-covered sample should exhibit a higher activity than the Pd-tipped sample, since the center part was covered by Pd. One explanation for this inconformity is the plasmon-induced charge transfer played a key role in the plasmon-enhanced catalysis rather than the photothermal heating. Therefore, the photothermal effect is not the main contribution in our reaction system.

The excited surface plasmons can also decay via the plasmon resonance energy transfer (PRET) process. The effect of PRET indicates the interaction of Pd with the SPR induced electric-field amplification localized nearby at the Au NR. To ascertain the region of electric field amplification upon SPR excitation and its possible contribution to the plasmon-induced enhancement, we performed the 3-D FDTD simulation to calculate the spatial distribution of electric field intensity as a function of incident polarization direction (Figure 7). Considering the random orientation of Pd−Au NRs in suspensions, two kinds of incident light polarization directions (parallel and

DOI: 10.1021/ja511719g
J. Am. Chem. Soc. 2015, 137, 948−957

perpendicular to the longitudinal direction of NR) were applied to the NRs. Surprisingly, the enhancement of electric field occurs at the tips of the NRs for both of the samples, regardless of the polarization direction. This suggests that only tip-coated Pd can be affected for the occurrence of plasmon resonance energy transfer. That is why the Pd-covered sample with extra laterally coated Pd did not show higher plasmon-enhanced activity. This result can direct us to utilize the SPR energy more efficiently, and also enables us to decrease the amount of Pd species by selective deposition only at the field-enhanced sites. Furthermore, due to the weak light absorption of Pd in the visible region, the PRET process is not the main process. The surface charge heterogeneity from electron transfer plays a key role in the enhanced catalytic reaction.

CONCLUSIONS

Anisotropic Pd-tipped and Pd-covered Au NRs have been successfully synthesized by a two-step seed-mediated growth method. The unique bimetallic NRs can act as the light absorber and the catalytically active site simultaneously, and exhibit plasmon-enhanced catalytic formic acid dehydrogenation at lower temperatures with higher performance compared with the conventional thermal catalysis. The nature of plasmon-enhanced thermal catalysis was studied at the single-particle level. By analyzing the energy relaxation path of plasmon-generated hot electrons, we confirmed the plasmon-induced interfacial interaction within these bimetal nanostructures, which is the main factor for the plasmon-enhanced catalytic activity. More importantly, the FDTD simulation shows that the SPR-induced enhancement is mainly located at the tips of the Au NRs, which can direct us to utilize the SPR energy more efficiently. The finding obtained here will help us to understand the nature of the plasmon-enhanced catalysis and offers a promising approach to integrate solar energy and conventional catalytic reactions.

ASSOCIATED CONTENT

Supporting Information

Additional results of structural characterizations, single-particle PL spectra, and catalytic activity tests of the samples. This material is available free of charge via the Internet at http://pubs.acs.org.

AUTHOR INFORMATION

Corresponding Author

*majima@sanken.osaka-u.ac.jp

Notes

The authors declare no competing financial interest.

ACKNOWLEDGMENTS

This work has been supported by Innovative Project for Advanced Instruments, Renovation Center of Instruments for Science Education and Technology, Osaka University, and a Grant-in-Aid for Scientific Research (Project 25220806) from the Ministry of Education, Culture, Sports, Science and Technology (MEXT) of the Japanese Government. We are thankful for the help of the Comprehensive Analysis Center of SANKEN, Osaka University. Z.Z. thanks the JSPS for a Postdoctoral Fellowship for Foreign Researchers (No. P13027).

REFERENCES

(1) Kudo, A.; Miseki, Y. *Chem. Soc. Rev.* **2009**, *38*, 253−278.
(2) Huang, X.; Li, Y.; Chen, Y.; Zhou, H.; Duan, X.; Huang, Y. *Angew. Chem., Int. Ed.* **2013**, *52*, 6063−6067.
(3) Kale, M. J.; Avanesian, T.; Christopher, P. *ACS Catal.* **2014**, *4*, 116−128.
(4) Liu, L. Q.; Ouyang, S. X.; Ye, J. H. *Angew. Chem., Int. Ed.* **2013**, *52*, 6689−6693.
(5) Tsao, Y.-C.; Rej, S.; Chiu, C.-Y.; Huang, M. H. *J. Am. Chem. Soc.* **2014**, *136*, 396−404.
(6) Linic, S.; Christopher, P.; Ingram, D. B. *Nat. Mater.* **2011**, *10*, 911−921.
(7) Kamat, P. V. *J. Phys. Chem. B* **2002**, *106*, 7729−7744.
(8) Tian, Y.; Tatsuma, T. *J. Am. Chem. Soc.* **2005**, *127*, 7632−7637.
(9) Tedsree, K.; Li, T.; Jones, S.; Chan, C. W. A.; Yu, K. M. K.; Bagot, P. A. J.; E. Marquis, A.; Smith, G. D. W.; Tsang, S. C. E. *Nat. Nanotechnol.* **2011**, *6*, 302−307.
(10) Jiang, K.; Xu, K.; Zou, S. Z.; Cai, W.-B. *J. Am. Chem. Soc.* **2014**, *136*, 4861−4864.
(11) Ni, W. H.; Kou, X. S.; Yang, Z.; Wang, J. F. *ACS Nano* **2008**, *2*, 677−686.
(12) Wang, Z. L.; Yan, J. M.; Ping, Y.; Wang, H. L.; Zheng, W. T.; Jiang, Q. *Angew. Chem., Int. Ed.* **2013**, *52*, 4406−4409.
(13) Tedsree, K.; Chan, C. W. A.; Jones, S.; Cuan, Q.; Li, W. K.; Gong, X. Q.; Tsang, S. C. E. *Science* **2011**, *332*, 224−228.
(14) Sarina, S.; Bai, S.; Huang, Y.; Chen, C.; Jia, J.; Jaatinen, E.; Ayoko, G. A.; Bao, Z.; Zhu, H. *Green Chem.* **2014**, *16*, 331−341.
(15) Wang, F.; Li, C.; Chen, H.; Jiang, R.; Sun, L.-D.; Li, Q.; Wang, J.; Yu, J. C.; Yan, C.-H. *J. Am. Chem. Soc.* **2013**, *135*, 5588−5601.
(16) Huang, X.; Li, Y.; Zhou, H.; Zhong, X.; Duan, X.; Huang, Y. *Chem.—Eur. J.* **2012**, *18*, 9505−9510.
(17) Zhou, X.; Choudhary, E.; Andoy, N. M.; Zou, N.; Chen, P. *ACS Catal.* **2013**, *3*, 1448−1453.
(18) Zheng, Z. K.; Tachikawa, T.; Majima, T. *J. Am. Chem. Soc.* **2014**, *136*, 6870−6873.
(19) Jana, N. R.; Gearheart, L.; Murphy, C. J. *Adv. Mater.* **2001**, *13*, 1389−1393.
(20) Nikoobakht, B.; El-Sayed, M. A. *Chem. Mater.* **2003**, *15*, 1957−1962.
(21) Johnson, P. B.; Christy, R. W. *Phys. Rev. B* **1972**, *6*, 4370−4379.
(22) Fan, F. R.; Liu, D. Y.; Wu, Y. F.; Duan, D.; Xie, Z. X.; Jiang, Z. Y.; Tian, Z. Q. *J. Am. Chem. Soc.* **2008**, *130*, 6949−6951.
(23) Grzelczak, M.; Pérez-Juste, J.; Rodríguez-González, B.; Liz-Marzán, L. M. *J. Mater. Chem.* **2006**, *16*, 3946−3951.
(24) Fennell, J.; He, D. S.; Tanyi, A. M.; Logsdail, A. J.; Johnston, R. L.; Li, Z. Y.; Horswell, S. L. *J. Am. Chem. Soc.* **2013**, *135*, 6554−6561.
(25) Xiang, Y. J.; Wu, X. C.; Liu, D. F.; Jiang, X. Y.; Chu, W. G.; Li, Z. Y.; Ma, Y.; Zhou, W. Y.; Xie, S. S. *Nano Lett.* **2006**, *6*, 2290.
(26) Zhang, X.; Su, Z. H. *Adv. Mater.* **2012**, *24*, 4574−4577.
(27) Guo, X.; Zhang, Q.; Sun, Y. H.; Zhao, Q.; Yang, J. *ACS Nano* **2012**, *6*, 1165−1175.
(28) Tokonami, S.; Morita, N.; Takasaki, K.; Toshima, N. *J. Phys. Chem. C* **2010**, *114*, 10336−10341.
(29) Toshima, N.; Ito, R.; Matsushita, T.; Shiraishi, Y. *Catal. Today* **2007**, *122*, 239−244.
(30) Gangula, A.; Podila, R.; Ramakrishna, M.; Karanam, L.; Janardhana, C.; Rao, A. M. *Langmuir* **2011**, *27*, 15268−15274.
(31) Chiu, C.-Y.; Yang, M.-Y.; Lin, F.-C.; Huang, J.-S.; Huang, M. H. *Nanoscale* **2014**, *6*, 7656−7665.
(32) Bouhelier, A.; Bachelot, R.; Lerondel, G.; Kostcheev, S.; Royer, P.; Wiederrecht, G. P. *Phys. Rev. Lett.* **2005**, *95*, 267405.
(33) Tcherniak, A.; Dominguez-Medina, S.; Chang, W.-S.; Swanglap, P.; Slaughter, L. S.; Landes, C. F.; Link, S. *J. Phys. Chem. C* **2011**, *115*, 15938−15949.
(34) Qiu, J. J.; Wei, W. D. *J. Phys. Chem. C* **2014**, *118*, 20735−20749.
(35) Govorov, A. O.; Richardson, H. H. *Nano Today* **2007**, *2*, 30−38.
(36) Chen, X.; Zhu, H.-Y.; Zhao, J.-C.; Zheng, Z.-F.; Gao, X.-P. *Angew. Chem., Int. Ed.* **2008**, *47*, 5353−5356.

DOI: 10.1021/ja511719g
J. Am. Chem. Soc. 2015, 137, 948−957

(37) Meng, X. G.; Wang, T.; Liu, L. Q.; Ouyang, S. X.; Li, P.; Hu, H. L.; Kako, T.; Iwai, H.; Tanaka, A.; Ye, J. H. *Angew. Chem., Int. Ed.* **2014**, *53*, 11478−11482.
(38) Govorov, A. O.; Zhang, W.; Skeini, T.; Richardson, H.; Lee, J.; Kotov, N. A. *Nanoscale Res. Lett.* **2006**, *1*, 84−90.
(39) Park, J.; Huang, J. Y.; Wang, W.; Murphy, C. J.; Cahill, D. G. *J. Phys. Chem. C* **2012**, *116*, 26335−26341.
(40) Baffou, G.; Quidant, R.; Girard, C. *Appl. Phys. Lett.* **2009**, *94*, 153109.

DOI: 10.1021/ja511719g
J. Am. Chem. Soc. 2015, 137, 948−957